

Chapter 2

Methods and Concepts

This chapter offers an introduction to the theoretical and experimental methods, which are important in the framework of this thesis. First, the concept of low-energy electron diffraction as a tool for surface structural investigations is outlined. Specifically, after a brief historical overview on the development of LEED in combination with its key features and challenges (Sect. 2.1.1), the typical experimental setup is illustrated (Sect. 2.1.2). In the following section, the basics of surface-diffraction theory are presented in view of the analysis performed in the time-resolved surface study of Chap. 6 (Sect. 2.2). For this purpose, the materials comprising the sample system are introduced (Sect. 2.3).

2.1 An Introduction to LEED

2.1.1 LEED Historical Context and Key Aspects

Low-energy electron diffraction is a technique for the structural investigation of crystalline surfaces based on the diffraction of electrons with low kinetic energy. The origins of LEED go back to the 1920s, when Davisson and Germer directed a beam of monochromatic, slow electrons at a nickel single-crystal under vacuum conditions [1]. They found that the recorded angular intensity pattern of the scattered electrons was in agreement with the concept of diffraction of wave-like electrons, as had recently been proposed by de Broglie [2]. At the same time, Thomson independently made similar observations with faster electrons in a backscattering as well as in a transmission geometry [3, 4].

These findings mark the beginning of modern electron diffraction experiments such as LEED, which then eventually developed into the powerful tool in surface crystallography it is today. With respect to the technique of X-ray diffraction from

crystals, which was already well-established at that time,¹ the use of electrons presented a few important advantages:

- X-rays are scattered relatively weakly by matter, resulting in large penetration depths, making electron-based methods far more sensitive to the surface structure.
- The energy of electrons can be easily adapted to fit the investigated sample, which is a far more involved task for most X-ray sources.
- Electronic and magnetic lens systems allow for a straight-forward manipulation and tailoring of the electron beam, while X-ray optics are challenging to produce.
- For the typical electron energies used for highest surface sensitivity, the electron wavelengths are comparable to the lattice spacing of most crystals, leading to large scattering angles.

Despite these advantages, the subsequent development of LEED came to an untimely end only few years later, owing largely to difficulties in meeting the requirements associated with the experimental setup. Specifically, high surface crystallinity as well as cleanliness of the sample both necessitated operation under ultrahigh vacuum conditions, which were not easily achievable at the time. Additionally, the lack of spatially-resolved detector systems and computational resources made LEED recordings arduous and time-consuming.

Only with the availability of suitable vacuum, electron sources and detection techniques in the 1960s, LEED achieved a wide acceptance as a surface probing tool within the scientific community. These advantages also in turn led to the development of the theoretical methods based on multiple scattering to allow for a quantitative understanding of the recorded data. With the technological requirements met, LEED rapidly became one of the standard methods for structure determination [6]. Nowadays, besides qualitative investigations on the symmetry and periodicity of a surface, the analysis of I-V curves and spot profiles in combination with robust numerical methods enables scientists to obtain detailed information about crystal defects as well as the precise atomic arrangement within a surface unit cell. Moreover, LEED setups are routinely coupled to Auger electron spectroscopy (AES), additionally yielding information about the chemical composition of surface contaminants [7].

2.1.2 *Experimental Setup*

LEED investigates the surface structure of a given crystalline sample by recording the scattered diffraction orders. Commonly, as shown in Fig. 2.1a, a collimated electron beam for sample probing is generated within a thermionic electron gun. The latter comprises a heated cathode filament and an electrostatic lens system, whereby LEED gun currents are typical in the range of 10^{-4} and 10^{-8} A [8]. The emitted electrons

¹The first quantitative X-ray bulk structural analysis was performed in 1913, only one year after the initial prove of X-ray diffraction [5].

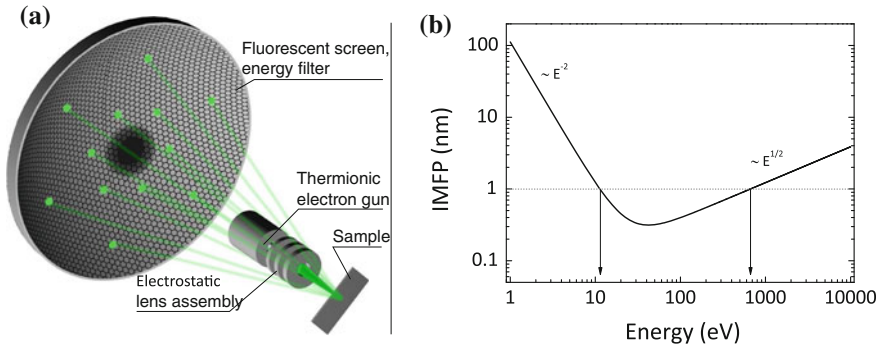


Fig. 2.1 Sketch of LEED principle and IMFP computation. **a** Electrons generated by a thermal emitter are focused on the sample by an electrostatic lens system. The (elastically) backscattered electrons are then recorded on a fluorescent screen after passing an energy filter (usually both shaped as a spherical cap). **b** Universal curve of IMFP for electrons in a solid [10]. Energy range with highest surface sensitivity below 1 nm indicated by arrows

are then backscattered by the sample and subsequently recorded on a spherical cap-shaped fluorescent phosphor screen. Since only the elastically scattered electrons carry the wanted structural information [9], an energy filter is employed to deflect any inelastically scattered electrons. The energy filter is most commonly made from a series of fine metal grids with the inner ones set to a retarding electrostatic potential just below the initial electron energy, allowing only elastically scattered electrons to pass.

Due to the use of low-energy electrons, LEED is extremely surface sensitive and has to be carried out under ultrahigh vacuum conditions to avoid sample contamination, e.g. through oxidation or adsorbed molecules. A plot of the inelastic mean-free-path (IMFP) as a function of the kinetic electron energy is shown in Fig. 2.1b [10] (for computation, see Appendix A.2). The minimal IMFP for most materials, including graphite, is found at electron energies of about 50 eV. Nevertheless, very high surface sensitivity with an IMFP below 1 nm is generally achieved for energies between 10 and 700 eV. This sensitivity stems from the collective excitation of vibrational lattice (phonons) and electron (plasmons) modes with energies between a few to some tens of electron volts above the Fermi level [11]. These excitations significantly reduce the typical penetration depth of impinging electrons by removing a substantial fraction of their initial kinetic energy.

Depending on the investigated quantity, LEED is operated in the following ways:

1. For a qualitative analysis of the surface structure in terms of lattice spacing, periodicity and symmetry, merely a reciprocal scale has to be determined to access these parameters directly. This can either be done by knowledge of the experiment's exact geometry or a reference diffraction pattern.

2. For a more quantitative analysis, the diffraction spot profile can be used to determine deviations from the ideal order, including the domain size (spot width) and the existence of steps, facets or surface defects (shape) [12, 13].
3. In order to extract information about the precise internal unit cell structure, the diffraction spot intensity is recorded as a function of electron energy (so-called *I-V curves*) [14–16]. An iterative approach based on the comparison with a theoretical model then leads to the atomic arrangement within the unit cell.

The combination of these analytical capabilities makes LEED into a versatile tool for detailed structural surface characterization.

2.2 Diffraction Pattern Formation in Two Dimensions

Diffraction can be seen as a result of the interaction between an incoming, periodic wave field and a likewise periodic array of scattering centers [11]. At large enough wave numbers k_0 of the incoming wave, the amplitudes of scattered waves are in-phase along certain directions (diffraction condition), resulting in an observable intensity on the detector. Normally, not only one but a larger number of conditions along different scattering directions are met simultaneously, resulting in the appearance of multiple beams and the so-called *diffraction pattern*.

To obtain a mathematical description of the process, we are assuming a monochromatic incoming plane wave as well as an infinite periodicity of the sample. This requirement is usually an adequate assumption in two dimensions with at most a few layers in the direction perpendicular to the surface, as well as an in-plane periodicity, which is limited only by either the domain size of the sample or the coherently probed area.

The surface periodicity is given in terms of a lattice. A lattice is defined as the simplest arrangement of points which follow the fundamental periodicity of the crystal [11]. Individual mesh cells of a lattice are called *unit cells* and carry the relationship between the lattice and the actual atomic positions (Fig. 2.2). Unit cells are chosen according to be the smallest possible repeating unit to fully describe the crystal structure. Depending on the actual atomic arrangement, different choices of unit cells are often possible to describe the same structure. A real space lattice is described by a set of two linearly independent lattice vectors defining the boundaries of the unit cell.

The above described diffraction condition, namely that a net flux of scattered waves is recorded along those directions, in which constructive interference occurs, is called the *Laue condition* and can be written as (Fig. 2.3)

$$a(\sin \Theta_n - \sin \Theta_0) = n\lambda, \quad (2.1)$$

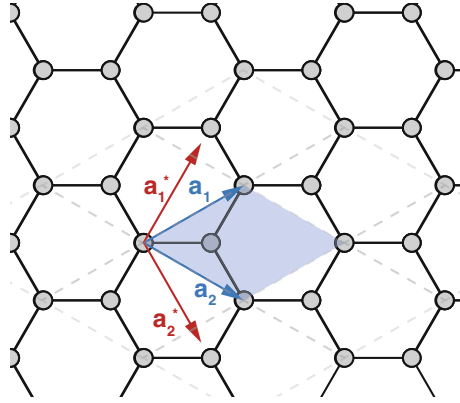


Fig. 2.2 Sketch of a single unit cell (blue) with lattice vectors \mathbf{a}_1 and \mathbf{a}_2 in case of a hexagonally symmetric surface atom arrangement. Dashed areas denote repeating unit cells. Reciprocal lattice vectors displayed in red

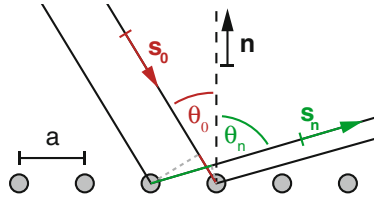


Fig. 2.3 Sketch of diffraction from a one-dimensional array of scatterers. Dashed black line denotes “surface” normal with unit vector \mathbf{n} . Incoming (outgoing) wave vector labeled \mathbf{s}_0 (\mathbf{s}_n). Red and green lines denote path length contributions ($a \sin \Theta_0$) and ($a \sin \Theta_n$), respectively. Lattice parameter: a

where Θ_0 and Θ_n are the angles of the incident and scattered waves, respectively, $n\lambda$ an integer multiple of the wavelength of the incoming wave, and $a = |\mathbf{a}|$ the lattice parameter.

When written in terms of the unit vectors \mathbf{s}_0 and \mathbf{s}_n of the incident and scattered beam, respectively, this expression becomes

$$\mathbf{a}(\mathbf{s}_n - \mathbf{s}_0) = \mathbf{a}\Delta\mathbf{s} = n\lambda. \quad (2.2)$$

Hence, the diffracted beam is determined by the normalized path length difference $\Delta\mathbf{s}$, which is given by integer multiples of $\lambda/|\mathbf{a}|$, a quantity proportional to the reciprocal lattice constant. Specifically, the reciprocal lattice vectors, \mathbf{a}_i^* , are defined in terms of the real space lattice vectors, \mathbf{a}_i , by the following relationship [17]:

$$\mathbf{a}_i^* = 2\pi \frac{\mathbf{a}_j \times \mathbf{n}}{|\mathbf{a}_i \times \mathbf{a}_j|}. \quad (2.3)$$

In Eq. 2.3, \mathbf{n} is the unit vector normal to the surface as depicted in Fig. 2.3. The relationship between real and reciprocal lattice vectors is often also expressed by $\mathbf{a}_i^* \cdot \mathbf{a}_j = 2\pi\delta_{ij}$ leading to the pairwise perpendicular vectors illustrated in Fig. 2.2.

Any general translation vector, relating two reciprocal lattice points, therefore takes the form

$$\mathbf{g}_{hk} = h\mathbf{a}_1^* + k\mathbf{a}_2^* = \Delta\mathbf{s}/\lambda. \quad (2.4)$$

The integers h and k are called *Miller indices*.

2.2.1 Ewald Construction

The above-mentioned diffraction criteria can be visualized by a geometrical construction called the *Ewald construction*. Before doing so, we will briefly assess the impact of two-dimensionality on the diffraction process.

From Eq. 2.3 one can see that whenever a real space lattice vector is increased in length, the corresponding reciprocal vector is decreased accordingly. Considering an isolated two-dimensional system, the lattice vector normal to the surface is infinitely stretched, hence the respective reciprocal lattice vector becomes infinitesimally small. This means that parallel to this direction, interference effects are eliminated, allowing the beam to be observed at all angles and energies. In the Ewald construction, this is expressed by the existence of reciprocal lattice rods rather than points for the direction normal to the surface (Fig. 2.4). As a consequence, a diffraction pattern of a quasi-two-dimensional system is seen at nearly any incident angle and energy.

In Fig. 2.4b, the Ewald sphere (in two dimensions) is shown for a single row of the surface reciprocal lattice depicted in Fig. 2.4a. The incident wave vector $\mathbf{k}_0 = 2\pi/\lambda$ (green arrow) impinges on the sample surface and is scattered (red arrows). As stated

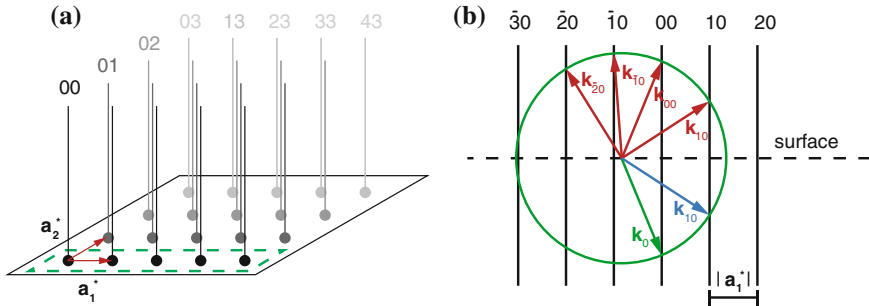


Fig. 2.4 Ewald construction. **a** Reciprocal space of a periodic surface with rods instead of points perpendicular to the surface. *Numbers above rods* Miller indices. *Red arrows* reciprocal unit vectors. *Green rectangle* denotes single row depicted in **(b)**. **b** Two-dimensional Ewald sphere. Incoming wave vector \mathbf{k}_0 in green, back-scattered (forward-scattered) wave vectors \mathbf{k}_{hk} in red (blue) with h and k Miller indices

earlier (Sect. 2.1.2), we are only concerned with the elastically scattered waves, since they carry the structural information of the sample system. If the scattered beams do not lose energy, they must have the same length as the incident wave vector, thus lying on a circle (sphere in three dimensions). Hence, the intersections of the circle of radius $|\mathbf{k}_0|$ with the lattice rods fulfill both the condition of energy conservation as well as the Laue diffraction condition.

The direct reflection from the incident beam is labeled \mathbf{k}_{00} and usually has to be blocked in order to observe the other, less intense diffracted beams. In the case of very thin samples or high electron energies, not only reflected, but also transmitted beams will be seen. Notably and in stark contrast to bulk diffraction, diffraction patterns will not only be observable for certain energy-angle relations, but basically for any chosen configuration, as long as the Ewald sphere's diameter is larger than the reciprocal lattice constant.

2.2.2 Overlayers and Domains

Based on the concept of the Ewald sphere, the total number of diffracted beams with their respective scattering angles can be determined for a given energy in combination with the knowledge of the reciprocal lattice. While the bulk structure of crystals is generally well known from x-ray crystallography, structural deviations of the surface from the bulk are quite common. Typical deviations may stem from surface reconstructions due to symmetry breaking and subsequent energy minimization or from the adsorption of molecules [11, 18]. This individual surface reconstruction will hereby strongly depend on the bulk structure, the type of molecules and bonds involved, as well as environmental factors such as temperature and pressure.

In the most general case, the lattice vectors of the overlayer or superstructure can be expressed in terms of the lattice vectors of the primary lattice [11]:

$$\mathbf{b}_1 = m_{11}\mathbf{a}_1 + m_{12}\mathbf{a}_2, \quad (2.5)$$

$$\mathbf{b}_2 = m_{21}\mathbf{a}_1 + m_{22}\mathbf{a}_2. \quad (2.6)$$

This can be rewritten in matrix notation as

$$\mathbf{b} = \begin{pmatrix} \mathbf{b}_1 \\ \mathbf{b}_2 \end{pmatrix} = \begin{pmatrix} m_{11} & m_{12} \\ m_{21} & m_{22} \end{pmatrix} \begin{pmatrix} \mathbf{a}_1 \\ \mathbf{a}_2 \end{pmatrix} = M\mathbf{a}. \quad (2.7)$$

Similarly, a relationship between the reciprocal lattices can be established

$$\mathbf{b}^* = M^*\mathbf{a}^*, \quad (2.8)$$

where the matrices M and M^* are related by [11]

$$\begin{pmatrix} m_{11} & m_{12} \\ m_{21} & m_{22} \end{pmatrix} = \frac{1}{\det M^*} \begin{pmatrix} m_{22}^* & -m_{21}^* \\ -m_{12}^* & m_{11}^* \end{pmatrix} \Leftrightarrow M(M^*)^T = 2\pi\mathbb{1}, \quad (2.9)$$

with $\mathbb{1}$ representing the identity matrix in two dimensions. Once the reciprocal lattice vectors of the superstructure are extracted from the diffraction pattern, its real space lattice vectors can in principle be computed. Nevertheless, this will only yield the periodicity of the overlayer, but not the information about its atomic arrangement or the registration to the surface. For an identification of the atom's positions within the unit cell, additional information needs to be included, e.g., from measurements of the I-V curves of the superstructure spots or by prior knowledge about preferred bonding sites of an adsorbate.

Frequently, more than one orientation of the superstructure is abundant. Such regions, which are comprising a certain orientation of the overlayer, are called domains or islands in case of very small coverage. Depending on the characteristic length scale of the domains, the probed sample area, and the coherence length of the source relative to each other, different results in term of observed diffraction patterns may be expected. When the domain size is comparable to the investigated sample area, the probe beam can in principle be scanned over the surface, yielding different diffraction patterns depending on the underlying domain orientation. In contrast, a domain size well below the size of the probed region leads to two distinguishable cases, depending on the ratio between coherence length l_c and domain size d :

1. $l_c < d$: A superposition of diffraction patterns from different domain orientations.
2. $l_c > d$: An interference between the diffraction signals from different domains.

Generally, the existence of domains can result in an additional ambiguity when interpreting the structure of the overlayer (see Fig. 2.5). In the diffraction pattern shown in Fig. 2.5A1, the clean surface (full circle) and overlayer (empty circle) spots have been identified. The overlayer is interpreted as a 2×2 superstructure (red unit cell), which translates to the real-space periodicity shown in Fig. 2.5B1. Alternatively, the same diffraction image (Fig. 2.5A2) can be understood as the superposition of three overlayer domain types as indicated in the real-space image in Fig. 2.5B2.

However, there exist several options for resolving this ambiguity in the interpretation of the diffraction patterns. For instance, the sample could be prepared in a way to allow only certain domain orientations, e.g., by the introduction of step defects [19]. Similarly, a piecewise scanning of small sample areas could reveal the abundance of domains.

When taking the diffraction pattern from surfaces or thin films with more than one atomic layer, the scattering from successive crystal planes has to be taken into account. In case of a rationally related overlayer, the lattice vectors can be expressed via Eqs. 2.5 and 2.6.

An incoming beam \mathbf{s}_0 (see Fig. 2.3) then produces a series of diffracted beams following the relation given in Eq. 2.4:

$$\mathbf{s}_0 - \mathbf{s}_{hk} = \lambda(h\mathbf{b}_1^* + k\mathbf{b}_2^*). \quad (2.10)$$

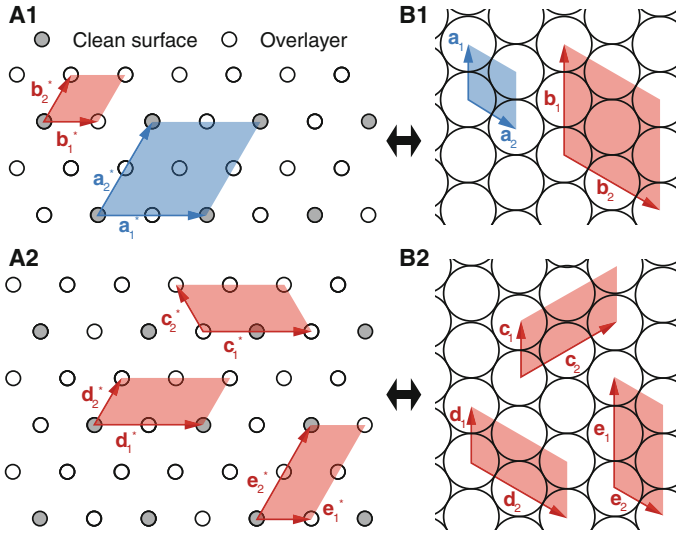


Fig. 2.5 Exemplary ambiguity in real-space superstructure lattice reconstruction. Clean surface (overlayer) unit cell(s) in blue (red). *Top panel* Interpretation as a single 2×2 overlayer structure. *Bottom panel*: Interpretation as a superposition of three 2×1 overlayer domains. Both real space superstructures shown in (B1) and (B2) result in the same diffraction pattern depicted in (A1) and (A2)

This beam is now incident upon another lattice plane, resulting in a new set of beams

$$\mathbf{s}_{hk} - \mathbf{s}_{fg} = \lambda(f\mathbf{a}_1^* + g\mathbf{a}_2^*), \text{ hence} \quad (2.11)$$

$$\mathbf{s}_0 - \mathbf{s}_{fg} = \lambda((f + hm_{11}^* + km_{21}^*)\mathbf{a}_1^* + (g + hm_{12}^* + km_{22}^*)\mathbf{a}_2^*), \quad (2.12)$$

with f, g, h, k, m_{xy}^* integers. Therefore, the beams \mathbf{s}_{fg} must correspond to the same set of angles as the \mathbf{s}_{hk} set. This also means that no new diffraction beams from scattering of successive planes will be introduced and multiple scattering in this case only shifts the intensities between diffraction spots.

2.3 Graphene and Graphene Technology

Whereas surfaces and in particular atomically thin superstructures can be seen as quasi-two-dimensional systems, free-standing 2D materials have not been available until very recently [20]. And even though there is now a vast number of monolayer systems available, including various types of oxides (e.g. BSCCO (“bisko”), $\text{Bi}_2\text{Sr}_2\text{Ca}_{n-1}\text{Cu}_n\text{O}_{2n+4+x}$) or chalcogenides (e.g. molybdenum disulfide, MoS_2), the material that continues to attract the most attention is graphene, a single crystalline sheet of carbon atoms [21].

One reason for the popularity of graphene as a research material are its outstanding electronic and mechanical properties as a consequence of its low dimensionality in combination with its atomic and electronic structure [22]. Specifically, the extremely high carrier mobility of graphene, even at elevated temperatures, motivates significant efforts in the field of graphene-based electronics. This includes, for example, the development of single-electron, high frequency transistors operating ballistically at room temperature [23–26] as well as devices for electromagnetic interference shielding [27]. Graphene-based applications are also under investigation in the fields of sensor development, biology and medical sciences [28, 29]. To date, however, most of these applications are not within immediate reach due to still existing challenges, mainly connected to the complexity of large-scale manufacturing of high-quality graphene sheets [28].

In contrast, the first applications using graphene as a compound material, in particular within a polymer matrix, are already available today [30–34]. So far, applications include graphene-based touch-screens [35–37], coatings for thermal and electromagnetic shielding and conductive ink.²

Yet, before graphene composite materials are discussed, a brief introduction to graphene is presented here. In view of the analysis performed in this work, this introduction will mainly focus on the structural properties of graphene. A broader and more general review of graphene can be found in Ref. [22, 28].

2.3.1 Structural Properties of Graphene

Graphene consists of a single layer of carbon atoms arranged in a hexagonal lattice with a two-atomic base (Fig. 2.6) [38]. The corresponding reciprocal lattice therefore also exhibits a six-fold symmetry with reciprocal lattice vectors as depicted in Fig. 2.5A.

The four binding electrons of each carbon atom hybridize into three covalent sp^2 bonds and a single, delocalized π bond [39]. The carbon-carbon bond length is 1.42 Å, leading to a unit cell vector length of $|\mathbf{a}_1| = |\mathbf{a}_2| = \sqrt{3} \cdot 1.42 \text{ Å} = 2.46 \text{ Å}$ [40]. The covalent bonding energy within the lattice plane is large ($E_{\text{inplane}} = 4.3 \text{ eV}$) compared to the van der Waals bonding energy between adjacent, stacked sheets in the case of graphite ($E_{\text{normal}} = 0.07 \text{ eV}$) [39]. The successful exfoliation of graphite to isolated single sheets of graphene can be attributed to this discrepancy [20].

Due to the honeycomb structure of the lattice, different types of grain boundaries for polycrystalline graphene are possible. Grain boundaries can in principle strongly influence the mechanical and electronic properties of the material by the formation of defects [41–43]. In the case of graphene, however, it was found that for large tilting angles the incorporation of defects into the crystal lattice does not necessarily lead to a drastic decrease in bond stability. In particular, tilting angles of 21.7°

²List of vendors of a selection of graphene-based applications can be found here: <http://www.understandingnano.com/graphene-companies.html>.

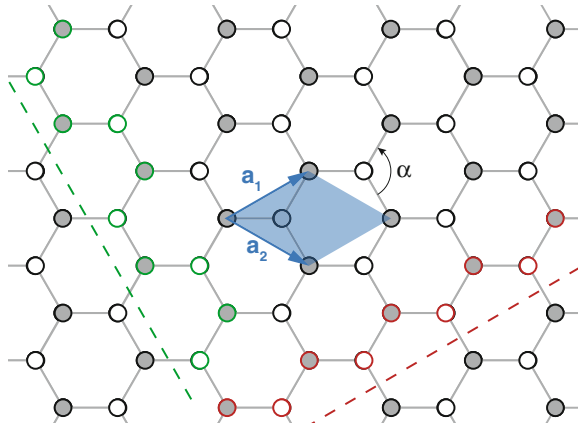


Fig. 2.6 Hexagonal lattice of graphene ($\alpha = 120^\circ$). Possible representation of the unit cell indicated in blue with unit cell vectors \mathbf{a}_1 and \mathbf{a}_2 . Atoms of the two sub-lattices are shaded with *dark* and *light gray*. Possible grain boundaries for polycrystalline graphene: Cut along $[10]$ direction leads to zigzag (*red*), cut along $[-12]$ direction leads to armchair configuration (*green*). Reciprocal lattice as in Fig. 2.5A

(zigzag configuration, red dashed line and atoms in Fig. 2.6) and 28.7° (armchair configuration, green dashed line and atoms in Fig. 2.6) lead to less initial strain on the carbon bonds compared to smaller angles in the same configuration, and are therefore very stable [43].

2.3.2 Polymers in Graphene Technology

As previously mentioned, potential graphene applications do not only arise from the use of pure graphene, but also from the combination of graphene with different other materials. For the latter case, two major current research areas can be identified, namely graphene-based heterostructures and composite materials.

Heterostructures describe a group of thin-film type materials, which are constructed by consecutive stacking of individual two-dimensional crystalline sheets on top of each other [21]. Whereas strong covalent bonds act within these sheets, the resulting heterostructures are held together by relatively weak van der Waals forces [44, 45].

The big appeal of such structures stems from the idea to atomically tailor material properties. With the large amount of readily available 2D crystals [21, 28], this provides for a seemingly endless number of possible combinations. Specific efforts are, for example, dedicated to find high temperature superconductors [21] or substituents for silicon-based electronics [46].

A conceptually similar approach to heterostructures is the manufacturing of composite materials. Here, too, the modification of material properties is in the foreground, which is commonly accomplished by immersion of graphene sheets or flakes (so called *nano-platelets*) in a polymer matrix [30, 31, 47–49]. From the technological point of view, graphene-based composite materials therefore offer one great advantage compared to heterostructures: Since they do not necessitate layer-based, large-area, high-quality, single-crystalline graphene, but mostly rely on nano-platelets of few to few tens of micrometers in diameter, the production process is greatly facilitated. At very low volumetric fractions of graphene, significant increases in tensile strength, Young's modulus, as well as thermal and electric conductivity have been reported [50]. The resulting features make these new materials interesting for a wide range of applications, as, for example, conductive plastics and ink as used in electromagnetic interference shielding [27], or implementation into energy conversion [51], energy storage [52] and non-volatile memory devices [53].

Polymers, including poly(methyl methacrylate) (PMMA) and polycarbonate (PC), are commonly used to stabilize the two-dimensional crystal sheets upon transfer from the substrate used in the preparation process [54] (Sect. 6.1.1). After the transfer process, the thin polymer film is removed by organic solvents such as acetone and isopropanol [55]. However, the strong physisorption of the polymer in contact with the graphene results in a very resistant ultrathin residual polymer layer [56, 57]. Several methods have been employed to remove this residual layer, e.g. changing the polymer [58], annealing at high temperatures [57], as well as polymer-free, so-called direct transfer [59]. However, to date, none of these approaches has resulted in large area, high quality graphene, stimulating additional interest in the investigation of the intimate connection between these two unlike materials [30, 60, 61].

2.3.3 Structural Properties of PMMA

PMMA is a lightweight plastic, which is most commonly known as acrylic glass (trade name: Plexiglas). Low cost and easy handling as well as the lack of potentially harmful bisphenol-A, as found in PC, allow PMMA to be used in many applications in medical technologies or as a resist in semiconductor electron beam lithography.

Structurally, this polymer consists of long chains of methyl-methacrylate (MMA) repeat units as shown in Fig. 2.7a, b. The molar mass of MMA is 100.12 g/mol, while the total polymer's molar mass strongly depends on the overall chain length, and is usually in the range of 5×10^4 – 10^6 g/mol.

PMMA molecules can display different tacticity, which describes the relative orientation of the side groups within the polymer. Possible configurations are isotactic (Fig. 2.7c), syndiotactic (Fig. 2.7d) and atactic (Fig. 2.7e). Tacticity strongly influences the physical properties of a polymer, including the degree to which it exhibits crystalline order.

STM as well as AFM studies have shown that thin PMMA Langmuir-Blodgett films on mica and graphite display long-range crystalline order independent of tac-

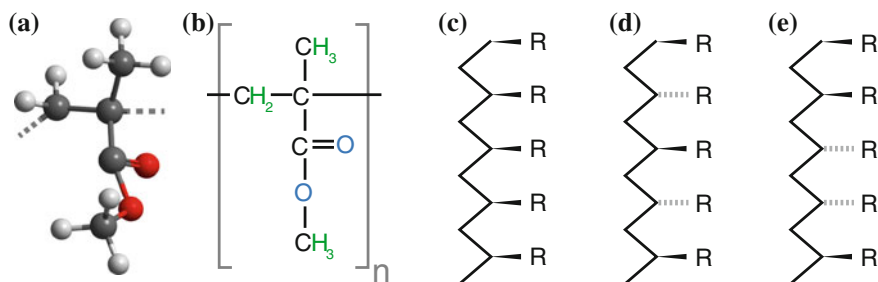


Fig. 2.7 Structure and tacticity of PMMA. **a, b** 3D model and structural formula of repeating monomer unit MMA. **c–e** Sketch of isotactic, syndiotactic and atactic configurations, respectively. *R* represents the functional (side) group of the monomer

ticity, in contrast to PMMA behavior in bulk [62, 63]. This behavior is in principle well known for other types of polymers, too, when subjected to a strong potential template [64, 65]. In the case of graphite and graphene, the adsorption of polymer chains to the surface is facilitated via van der Waals forces, similar to the bonding between consecutive graphene planes [66].

Atactic and syndiotactic PMMA molecules both arrange in a folded-chain configuration with little to no backbone crossovers [62]. The chain-to-chain distances reported in the literature are 5.0(1.0) and 4.8(1.9) Å, respectively, with a repeating monomer unit length of about 2.5 Å in direction of the polymer backbone. In the case of isotactic PMMA, linear as well as helical arrangements are found with a somewhat smaller interchain distance of the latter of 3.7(0.8) Å [62, 67, 68].

Because of the sensitivity of PMMA to electron irradiation, the formation of crystalline folded-chain conformations is challenging to observe in a regular transmission electron microscope (TEM), because of the relatively high electron current density of such systems. For ULEED, a quantitative analysis of the degradation behavior can be found in Appendix B.4.

References

1. Davisson D, Germer LH (1927) Diffraction of electrons by a crystal of nickel. *Phys Rev* 30(6):705–740. http://prola.aps.org/abstract/PR/v30/i6/p705_1
2. De Broglie L (1924) *Recherches sur la théorie des quanta*. Phd thesis, Université Paris-Sorbonne, Paris. <http://tel.archives-ouvertes.fr/docs/00/04/70/78/PDF/tel-00006807.pdf>
3. Thomson GP, Reid A (1927) Diffraction of cathode rays by a thin film. *Nature* 119(3007):890. <http://adsabs.harvard.edu/abs/1927Natur.119Q.890T>
4. Thomson GP (1928) Experiments on the diffraction of cathode rays. *Proc R Soc A* 117(778):600–609. <http://web.pdx.edu/pmoeck/pdf/Thomson1928.pdf>
5. Bragg WL (1912) The specular reflection of X-rays. *Nature* 90(2250):410. <http://adsabs.harvard.edu/abs/1912Natur.90.410B>

6. Watson PR, Van Hove MA, Hermann K (2002) NIST surface structure database. National institute of standards and technology. <http://chemistry.oregonstate.edu/personalhomepages/Watson/Research/SSD.htm>
7. Auger P (1925) Sur les rayons B secondaires produit dans un gaz par des rayons X. *C R Phys* 180:65–73
8. Van Hove MA, Weinberg WH, Chan CM (1986) Low-energy electron diffraction, 1st edn. Springer, Heidelberg
9. Williams DB, Carter CB, Barry C (2009) Transmission electron microscopy: a textbook for materials science, 2nd edn. Springer, New York
10. Adams DL, Nielsen HB, Van Hove MA (1979) Quantitative analysis of low-energy-electron diffraction: application to Pt(111). *Phys Rev B* 20(12):4789–4806. <http://journals.aps.org/prb/abstract/10.1103/PhysRevB.20.4789>
11. Clarke LJ (1985) Surface crystallography: an introduction to low energy electron diffraction, 1st edn. Wiley, New York
12. Scheithauer U, Meyer G, Henzler M (1986) A new LEED instrument for quantitative spot profile analysis. *Surf Sci* 178(1–3):441–451. <http://www.sciencedirect.com/science/article/pii/0039602886903213>
13. Minoda H, Shimakura T, Yagi K, Meyer F, Horn Von Hoegen M (1999) Gold-induced faceting on an Si(hhm) surface (m/h=1.4–1.5) studied by spot profile analyzing low-energy electron diffraction. *Surf Sci* 432(1–2):69–80. <http://www.sciencedirect.com/science/article/pii/S0039602899005166>
14. Debe MK, King DA (1982) The reliability of LEED I-V spectra: incidence angle errors and symmetry effects on W (100)(1*1). *J Phys C: Solid State Phys* 15(10):2257. <http://iopscience.iop.org/0022-3719/15/10/025>
15. Held G, Pfnür H, Menzel D (1992) A LEED-IV investigation of the Ru (001)-p (2x1)-H structure. *Surf Sci* 271(1–2):21–31. <http://www.sciencedirect.com/science/article/pii/0039602892908584>
16. Urano T, Kanaji T, Kaburagi M (1983) Surface structure of MgO (001) surface studied by LEED. *Surf Sci* 134(1):109–121. <http://www.sciencedirect.com/science/article/pii/003960288390314X>
17. Lüth H (2001) Solid surfaces, interfaces and thin films, 4th edn. Springer, New York
18. Henzler M, Göpel W (1994) Oberflächenphysik des Festkörpers, 2nd edn. B. G. Teubner, Berlin
19. Pantel R, Bujor M, Bardolle J (1979) Oxygen adsorption on various vicinal faces close to the (0001) basal plane of rhenium. *Surf Sci* 83(1):228–242. <http://www.sciencedirect.com/science/article/pii/0039602879904898>
20. Novoselov KS, Geim AK, Morozov SV, Jiang D, Zhang Y, Dubonos SV, Grigorieva IV, Firsov AA (2004) Electric field effect in atomically thin carbon films. *Science* 306(5696):666–669. ISSN 1095-9203. <http://www.ncbi.nlm.nih.gov/pubmed/15499015>
21. Geim AK, Grigorieva IV (2013) Van der Waals heterostructures. *Nature* 499(7459):419–425. ISSN 1476-4687. <http://www.ncbi.nlm.nih.gov/pubmed/23887427>
22. Geim AK, Novoselov KS (2007) The rise of graphene. *Nat Mater* 6(3):183–191. ISSN 1476-1122. <http://www.nature.com/nmat/journal/v6/n3/abs/nmat1849.html>
23. Geim AK, Novoselov KS (2012) Towards graphene-based electronics. Technical report, Centre for Mesoscience and Nanotechnology, Manchester. <http://oai.dtic.mil/oai/oai?verb=getRecord&metadataPrefix=html&identifier=ADA554986>
24. Lin YM, Dimitrakopoulos C, Jenkins KA (2010) 100-GHz transistors from wafer-scale epitaxial graphene. *Science* 327(5966):662. <http://www.sciencemag.org/content/327/5966/662.short>
25. Kim K, Choi J-Y, Kim T, Cho S-H, Chung H-J (2011) A role for graphene in silicon-based semiconductor devices. *Nature* 479(7373):338–344. ISSN 1476-4687. <http://www.ncbi.nlm.nih.gov/pubmed/22094694>
26. Son Y-W, Cohen ML, Louie SG (2006) Energy gaps in graphene nanoribbons. *Phys Rev Lett* 97(21):216803. ISSN 0031-9007. <http://link.aps.org/doi/10.1103/PhysRevLett.97.216803>

27. Zhang H-Bi, Yan Q, Zheng W-G, He Z, Yu Z-Z (2011) Tough graphene-polymer microcellular foams for electromagnetic interference shielding. *ACS Appl Mater Interfaces* 3(3):918–924. ISSN 1944-8244. <http://www.ncbi.nlm.nih.gov/pubmed/21366239>
28. Novoselov KS, Fal'ko VI, Colombo L, Gellert PR, Schwab MG, Kim K (2012) A roadmap for graphene. *Nature* 490(7419):192–200. ISSN 1476-4687. <http://www.ncbi.nlm.nih.gov/pubmed/23060189>
29. Xia F, Mueller T, Lin Y-M, Valdes-Garcia AI, Avouris P (2009) Ultrafast graphene photodetector. *Nat Nanotechnol* 4(12):839–843. ISSN 1748-3395. <http://www.ncbi.nlm.nih.gov/pubmed/19893532>
30. Ramanathan T, Abdala AA, Stankovich S, Dikin DA, Herrera-Alonso M, Piner RD, Adamson DH, Schniepp HC, Chen X, Ruoff RS, Nguyen ST, Aksay IA, Prud'Homme RK, Brinson LC (2008) Functionalized graphene sheets for polymer nanocomposites. *Nat Nanotechnol* 3(6):327–331. ISSN 1748-3395. <http://www.ncbi.nlm.nih.gov/pubmed/18654541>
31. Stankovich S, Dikin DA, Dommett GHB, Kohlhaas KM, Zimney EJ, Stach EA, Piner RD, Nguyen ST, Ruoff RS (2006) Graphene-based composite materials. *Nature* 442(7100):282–286. ISSN 1476-4687. <http://www.ncbi.nlm.nih.gov/pubmed/16855586>
32. Xu Y, Wang Y, Liang J, Huang Y, Ma Y, Wan X, Chen Y (2009) A hybrid material of graphene and poly (3,4-ethyldioxythiophene) with high conductivity, flexibility, and transparency. *Nano Res* 2(4):343–348. ISSN 1998-0124. <http://link.springer.com/10.1007/s12274-009-9032-9>
33. Lee YR, Raghu AV, Jeong HM, Kim BK (2009) Properties of waterborne polyurethane/functionalized graphene sheet nanocomposites prepared by an in situ method. *Macromol Chem Phys* 210(15):1247–1254. <http://onlinelibrary.wiley.com/doi/10.1002/macp.200900157/full>
34. Quan H, Zhang B, Zhao Q, Yuen RKK, Li RKY (2009) Facile preparation and thermal degradation studies of graphite nanoplatelets (GNPs) filled thermoplastic polyurethane (TPU) nanocomposites. *Compos Part A: Appl Sci Manuf* 40(9):1506–1513. <http://www.sciencedirect.com/science/article/pii/S1359835X09001845>
35. Bae S, Kim H, Lee Y, Xu X, Park J-S, Zheng Y, Balakrishnan J, Lei T, Kim HR, Song YI, Kim Y-J, Kim KS, Ozyilmaz B, Ahn J-H, Hong BH, Iijima S (2010) Roll-to-roll production of 30-inch graphene films for transparent electrodes. *Nat Nanotechnol* 5(8):574–578. ISSN 1748-3395. <http://www.ncbi.nlm.nih.gov/pubmed/20562870>
36. Kim KS, Zhao Y, Jang H, Lee SY, Kim JM, Ahn J-H, Kim P, Choi J-Y, Hong BH (2009) Large-scale pattern growth of graphene films for stretchable transparent electrodes. *Nature* 457(7230):706–710. ISSN 1476-4687. <http://www.ncbi.nlm.nih.gov/pubmed/19145232>
37. Ryu J, Kim Y, Won D, Kim N, Park JS, Lee E-K, Cho D, Cho S-P, Kim SJ, Ryu GH, Shin H-A-S, Lee Z, Hong BH, Cho S (2014) Fast synthesis of high-performance graphene films by hydrogen-free rapid thermal chemical vapor deposition. *ACS Nano* 8(1):950–956. ISSN 1936-086X. <http://www.ncbi.nlm.nih.gov/pubmed/24358985>
38. Bostwick A, Ohta T, Seyller T, Horn K, Rotenberg E (2007) Quasiparticle dynamics in graphene. *Nat Phys* 3(1):36–40. ISSN 1745-2473. <http://www.nature.com/doi/10.1038/nphys477>
39. Trauzettel T (2007) Von Graphit zu Graphen. *Phys J* 6(7):39–44. www.pro-physik.de/details/articlePdf/1104875/issue.html
40. Baskin Y, Meyer L (1955) Lattice constants of graphite at low temperatures. *Phys Rev* 100(2):544. http://prola.aps.org/abstract/PR/v100/i2/p544_1
41. Yazyev OV, Louie SG (2010) Topological defects in graphene: dislocations and grain boundaries. *Phys Rev B* 81(19):195420. ISSN 1098-0121. <http://link.aps.org/doi/10.1103/PhysRevB.81.195420>
42. Huang PY, Ruiz-Vargas CS, van der Zande AM, Whitney WS, Levendorf MP, Kevek JW, Garg S, Alden JS, Hustedt CJ, Zhu Y, Park J, McEuen PL, Muller DA (2011) Grains and grain boundaries in single-layer graphene atomic patchwork quilts. *Nature* 469(7330):389–392. ISSN 1476-4687. <http://www.ncbi.nlm.nih.gov/pubmed/21209615>
43. Grantab R, Shenoy VB, Ruoff RS (2010) Anomalous strength characteristics of tilt grain boundaries in graphene. *Science* 330(6006):946–948. ISSN 1095-9203. <http://www.ncbi.nlm.nih.gov/pubmed/21071664>

44. Ponomarenko LA, Geim AK, Zhukov AA, Jalil R, Morozov SV, Novoselov KS, Grigorieva IV, Hill EH, Cheianov VV, Fal'ko VI, Watanabe K, Taniguchi T, Gorbachev RV (2011) Tunable metal-insulator transition in double-layer graphene heterostructures. *Nat Phys* 7(12):958–961. ISSN 1745-2473. <http://www.nature.com/doi/10.1038/nphys2114>
45. Haigh SJ, Gholinia A, Jalil R, Romani S, Britnell L, Elias DC, Novoselov KS, Ponomarenko LA, Geim AK, Gorbachev R (2012) Cross-sectional imaging of individual layers and buried interfaces of graphene-based heterostructures and superlattices. *Nat Mater* 11(9):764–767. ISSN 1476-1122. <http://www.ncbi.nlm.nih.gov/pubmed/22842512>
46. Britnell L, Gorbachev RV, Jalil R, Belle BD, Schedin F, Mishchenko A, Georgiou T, Katsnelson MI, Eaves L, Morozov SV, Peres NMR, Leist J, Geim AK, Novoselov KS, Ponomarenko LA (2012) Field-effect tunneling transistor based on vertical graphene heterostructures. *Science* 335(6071):947–950. ISSN 1095-9203. <http://www.ncbi.nlm.nih.gov/pubmed/22300848>
47. Das TK, Prusty S (2013) Graphene-based polymer composites and their applications. *Polym-Plast Technol Eng* 52(4):319–331. ISSN 0360-2559. <http://www.tandfonline.com/doi/abs/10.1080/03602559.2012.751410>
48. Hasan T, Scardaci V, Tan PH, Bonaccorso F, Rozhin AG, Sun Z, Ferrari AC (2011) *Molecular- and nano-tubes*, 1st edn. Springer, New York
49. Choi KS, Liu F, Choi JS, Seo TS (2010) Fabrication of free-standing multilayered graphene and poly(3,4-ethylenedioxythiophene) composite films with enhanced conductive and mechanical properties. *Langmuir* 26(15):12902–12908. ISSN 1520-5827. <http://www.ncbi.nlm.nih.gov/pubmed/20617852>
50. Du J, Cheng HM (2012) The fabrication, properties, and uses of graphene/polymer composites. *Macromol Chem Phys* 213(10–11):1060–1077. <http://onlinelibrary.wiley.com/doi/10.1002/macp.201200029/full>
51. Kamat PV (2011) Graphene-based nanoassemblies for energy conversion. *J Phys Chem Lett* 2(3):242–251. ISSN 1948-7185. <http://pubs.acs.org/doi/abs/10.1021/jz101639v>
52. Sun Y, Shi G (2013) Graphene/polymer composites for energy applications. *J Polym Sci Part B: Polym Phys* 51(4):231–253. ISSN 08876266. <http://doi.wiley.com/10.1002/polb.23226>
53. Lara-Avila S, Moth-Poulsen K, Yakimova R, Bjørnholm T, Fal'ko V, Tzalenchuk A, Kubatkin S (2011) Non-volatile photochemical gating of an epitaxial graphene/polymer heterostructure. *Adv Mater* 23(7):878–882. ISSN 1521-4095. <http://www.ncbi.nlm.nih.gov/pubmed/21328484>
54. Li X, Zhu Y, Cai W, Borysiak M, Han B, Chen D, Piner RD, Colombo L, Ruoff RS (2009) Transfer of large-area graphene films for high-performance transparent conductive electrodes. *Nano Lett* 9(12):4359–63. ISSN 1530-6992. URL <http://www.ncbi.nlm.nih.gov/pubmed/19845330>
55. Reina A, Jia X, Ho J, Nezich D, Son H, Bulovic V, Dresselhaus MS, Kong J (2009) Large area, few-layer graphene films on arbitrary substrates by chemical vapor deposition. *Nano Lett* 9(1):30–5. ISSN 1530-6984. <http://www.ncbi.nlm.nih.gov/pubmed/19046078>
56. Lin Y-C, Jin C, Lee J-C, Jen S-F, Suenaga K, Chiu P-W (2011) Clean transfer of graphene for isolation and suspension. *ACS Nano* 5(3):2362–8. ISSN 1936-086X. <http://www.ncbi.nlm.nih.gov/pubmed/21351739>
57. Lin Y-C, Lu CC, Yeh CH, Jin C (2012) Graphene annealing: how clean can it be? *Nano Lett* 12(1):414–419. <http://pubs.acs.org/doi/abs/10.1021/nl203733r>
58. Park HJ, Meyer J, Roth S, Skákalová V (2010) Growth and properties of few-layer graphene prepared by chemical vapor deposition. *Carbon* 48(4):1088–1094. <http://www.sciencedirect.com/science/article/pii/S0008622309007659>
59. Regan W, Alem N, Alemán B, Geng B, Girit C, Maserati L, Wang F, Crommie M, Zettl A (2010) A direct transfer of layer-*a* graphene. *Appl Phys Lett* 96(11):113102. ISSN 00036951. <http://scitation.aip.org/content/aip/journal/apl/96/11/10.1063/1.3337091>
60. Kuilla T, Bhadra S, Yao D, Kim NH (2010) Recent advances in graphene based polymer composites. *Prog Polym Sci* 35(11):1350–1375. <http://www.sciencedirect.com/science/article/pii/S0079670010000699>
61. Rissanou AN, Harmandaris V (2014) Dynamics of various polymer-graphene interfacial systems through atomistic molecular dynamics simulations. *Soft Matter* 10(16):2876–2888. ISSN 1744-6848. <http://www.ncbi.nlm.nih.gov/pubmed/24667937>

62. Ha JS, Roh H-S, Jung S-D, Park S-J, Kim J-J, Lee E-H (1994) Structural study of a poly(methylmethacrylate) Langmuir-Blodgett film on a graphite surface by scanning tunneling microscope. *J Vac Sci Technol B: Microelectron Nanometer Struct* 12(3):1977. ISSN 0734211X. <http://link.aip.org/link/?JVVB/12/1977/1&Agg=doi>
63. Takanashi Y, Kumaki J (2013) Significant melting point depression of two-dimensional folded-chain crystals of isotactic poly(methyl methacrylate)s observed by high-resolution in situ atomic force microscopy. *Phys Chem B* 117(18):5594–5605. <http://www.ncbi.nlm.nih.gov/pubmed/23614490>
64. McGonigal GC, Bernhardt RH, Yeo YH, Thomson DJ (1991) Observation of highly ordered, two-dimensional n-alkane and n-alkanol structures on graphite. *J Vac Sci Technol B*, 9(2):1107. ISSN 0734211X. <http://scitation.aip.org/content/avs/journal/jvstb/9/2/10.1116/1.585270>
65. Hoffman D, Miller L (1997) Kinetics of crystallization from the melt and chain folding in polyethylene fractions revisited: theory and experiment. *Polymer* 38(13):3151–3212. <http://www.sciencedirect.com/science/article/pii/S0032386197000712>
66. Ibach H (2006) *Physics of surfaces and interfaces*, 1st edn. Springer, New York
67. Brinkhuis RHG, Schouten AJ (1991) Thin-film behavior of poly(methyl methacrylates). 1. Monolayers at the air-water interface. *Macromolecules* 24(7):1487–1495. <http://pubs.acs.org/doi/abs/10.1021/ma00007a009>
68. Brinkhuis RHG, Schouten AJ (1991) Thin-film behavior of poly(methyl methacrylates). 2. An FT-IR study of Langmuir-Blodgett films of isotactic PMMA. *Macromolecules* 24(7):1496–1504. <http://pubs.acs.org/doi/abs/10.1021/ma00007a010>

Development of an Ultrafast Low-Energy Electron
Diffraction Setup

Gulde, M.

2015, XVII, 138 p. 62 illus., 28 illus. in color., Hardcover

ISBN: 978-3-319-18560-6